

Pressure dependence of the laser-metal interaction under laser powder bed fusion conditions probed by *in situ* X-ray imaging

Nicholas P. Calta^{a,*}, Aiden A. Martin^a, Joshua A. Hammons^a, Michael H. Nielsen^a,
Tien T. Roehling^a, Kamel Fezzaa^b, Manyalibo J. Matthews^a, Jason R. Jeffries^a, Trevor M. Willey^a,
Jonathan R.I. Lee^{a,*}

^a Physical and Life Sciences Directorate, Lawrence Livermore National Laboratory, 7000 East Avenue, Livermore, CA, 94550, United States

^b X-ray Science Division, Argonne National Laboratory, 9700 S Cass Avenue, Argonne, IL, 60439, United States

ARTICLE INFO

Keywords:

Additive manufacturing
Laser powder bed fusion
Surface tension
Pressure
Laser material interaction

ABSTRACT

Laser powder bed fusion (LPBF) additive manufacturing and laser welding are powerful metal processing techniques with broad applications in advanced sectors such as the biomedical and aerospace industries. One common process variable that can tune laser-material interaction dynamics in these two techniques is adjustment of the composition and pressure of the atmosphere in which the process is conducted. While some of the physical mechanisms that are governed by the ambient pressure are well known from the welding literature, it remains unclear how these mechanisms extend to the distinct process conditions of LPBF. *In situ* studies of the differences in subsurface structure and behavior are essential for understanding the effects of gas pressure and composition on the LPBF processes. This article reports the use of *in situ* X-ray imaging to directly probe the morphological evolution of the liquid-vapor interface during laser melting as a function of ambient pressure and oxygen partial pressure under LPBF conditions in 316 L steel, Ti-64, aluminum 6061, and Nickel 400. We observe significant changes in melt pool morphology as a function of pressure. Furthermore, similar changes in morphology occur due to an increase in oxygen partial pressure in the process atmosphere. Temperature- and composition-dependent changes in surface tension of the liquid metal drive this change in behavior, which has the potential to influence defect creation and final morphology in LPBF parts.

1. Introduction

Laser powder bed fusion (LPBF) additive manufacturing relies on a high-power laser to melt thin layers of metal powder into a specific 2D shape. This process is then repeated hundreds to thousands of times to produce a 3D part in a layer-by-layer fashion. While industrial adoption of this technology is accelerating [1], unanswered questions remain about the detailed mechanisms that govern the laser-material interaction central to the process. While a good deal of insight is transferrable from existing laser welding literature, most LPBF occurs in a different processing regime than typical laser welding conditions so the governing mechanisms are subtly different [2].

One common process variable used to influence laser weld characteristics is the ambient pressure [3]. Adjusting the pressure of the cover gas has a significant influence on weld depth at slow scan speeds typical of laser welding, but this influence diminishes at higher scan speeds more typical of LPBF [4,5]. These fluid dynamics have been

extensively investigated in the context of welding, where at sufficiently low scan speeds the melt depth under vacuum can be twice as much as that observed at atmospheric pressure [5]. The behavior in the slow scanning regime has been investigated by *ex situ* sample analysis to determine melt depth [4,6], *in situ* X-ray imaging [7–9], *in situ* optical imaging [10–12], and modelling [6,13] in the context of laser welding, with studies primarily focused on the deep penetration regime relevant to keyhole welding. The melt pool depth is ultimately governed by vapor depression depth, which is primarily influenced by the balance between vapor recoil pressure of metal vaporization and the surface tension of the liquid metal [6,13–15]. High speed optical imaging [16] and studies of powder denudation [17] illustrate powder is blown away from the melt pool at low pressure, while it is entrained in the gas flow and drawn inward towards the melt at high pressure. This difference is due to changes in the balance between expansion of the metal vapor plume and gas entrainment of the surrounding Ar cover gas present at atmospheric pressures. However, the subsurface dynamics and vapor

* Corresponding authors.

E-mail addresses: calta1@llnl.gov (N.P. Calta), lee204@llnl.gov (J.R.I. Lee).

<https://doi.org/10.1016/j.addma.2020.101084>

Received 9 October 2019; Received in revised form 27 December 2019; Accepted 19 January 2020

Available online 23 January 2020

2214-8604/ © 2020 The Authors. Published by Elsevier B.V. This is an open access article under the CC BY license (<http://creativecommons.org/licenses/by/4.0/>).

depression behavior have not been investigated in detail as a function of pressure in the fast scanning regime. Understanding changes to melt pool flow is essential to understand the solidification conditions of the welded region and the resulting microstructure, which ultimately dictates the properties of the final part.

High speed X-ray imaging probes subsurface fluid dynamics that cannot be directly observed with other *in situ* tools and has been applied to both laser welding [7–9,18] and LPBF [19–21]. X-ray imaging experiments based on both synchrotron and laboratory sources have investigated keyhole dynamics [8,22], pore formation [23], and hot cracking in deep penetration laser welding [7]. Recent imaging studies focused on the LPBF process have investigated high speed phenomena related to keyhole dynamics and pore formation [24], keyhole geometry as a function of laser scan parameters in Ti-6Al-4 V (Ti-64) [25], the correlation between vapor depression shape and spatter behavior [26], solidification dynamics in spot welding [20], pore formation dynamics due to scan geometry effects [27], and melt behavior in deep powder beds [21]. While some of these studies used variable pressure conditions during their investigations [24], none explicitly investigated the influence of cover gas pressure and composition on the melt pool dynamics observed. In this article, we use high speed X-ray imaging to probe changes in the laser-material interaction relevant to both laser welding and LPBF as a function of both laser scan parameters and ambient pressure. These experiments include studies of 316 L steel, Ti-64, Nickel 400, and Al6061 under vacuum, ~ 97 kPa high purity Ar, and ~ 97 kPa Ar with 13,000 ppm O₂ partial pressure. The behavior of the vapor-liquid interface significantly changes under vacuum conditions and atmospheric pressure Ar cover gas. These differences are primarily caused by changes in flow behavior and surface tension dominated by changes in surface temperature of the melt pool as a function of pressure. Additional experiments probe the effects of oxygen partial pressure on LPBF melt pool dynamics. Increases in oxygen partial pressure induce subtle but similar changes to the vapor-liquid interface, highlighting the importance of surface tension changes due to either temperature or oxygen content in determining melt pool behavior.

2. Methods

Transmission X-ray imaging experiments were performed using a custom-built LPBF testbed system described in detail by Martin et al. [24]. It consists of a vacuum chamber with an anti-reflective coated optical window for the laser to enter and Be windows on each side to allow the X-ray beam to transmit through the chamber. A 1070 nm continuous wave (CW) process laser (IPG Photonics, YLR-500-AC) was directly coupled via a collimator (IPG Photonics, D25) to a three-axis galvanometer scanner system (Nutfield Technologies, 3XB scan head), which directed the process laser to the sample position inside the LPBF testbed chamber. Laser powers reported here refer to output power at the laser and expected optical losses through the system are estimated to be $\sim 3\%$. The experiments used two slightly different beam diameters: $45 \pm 5 \mu\text{m}$ and $55 \pm 5 \mu\text{m}$ (D4 σ , or $1/e^2$ diameter for a perfectly Gaussian beam). Pressure was monitored by a Piezo and Micro Pirani combination pressure gauge (MKS Instruments, 910 DualTrans) and regulated by a mass flow controller for the addition of Ar gas and a turbo molecular vacuum pump (Pfeiffer HiCube 80). Oxygen partial pressure was monitored by an oxygen vacuum probe (XS22, ZIROX Sensoren und Elektronik GmbH). Samples were aligned to the X-ray beam with translation stages (Attocube, AG) positioned inside the vacuum chamber. Samples consisted of a single plate of 316 L stainless steel (380 μm or 508 μm , Maudlin & Son Mfg. Co., Inc.), Nickel 400 alloy (508 μm , United States Brass & Copper, 28–34 % Cu, < 2.5 % Fe, < 2 % Mn, < 0.5 % Si, < 0.3 % C, balance Ni), aluminum 6061 (635 μm , ThyssenKrupp Materials NA, Inc.) or Ti-64 alloy (508 μm , Performance Titanium Group) sandwiched between two 300 μm thick glassy carbon plates (22 grade, SPI Supplies) held in place by set screws.

In some instances, the glassy carbon plates were not used and only the metal sample was secured in place with the set screws. Two thicknesses of 316 L steel plates were used as samples, and comparisons at 800 mm/s to determine the effect of thermal boundary conditions observed negligible differences in vapor depression behavior at powers up to 400 W. After a sample was placed in the chamber, it was evacuated to less than 0.13 kPa and subsequently either (i) backfilled with Ar (ultra high purity, 99.999 %) and maintained at a pressure between 93 and 100 kPa under a constant Ar gas flow of 500 standard cubic centimeters per minute (sccm) combined with dynamic purging using a roughing pump (ambient), (ii) backfilled with Ar, opened the chamber door to admit a significant volume of air to the chamber, then closed the door and held at a constant pressure of ~ 101 kPa under a constant Ar gas flow of 500 sccm (oxygen poisoned), or (iii) continuously evacuated with a turbo pump until the pressure reached less than 1.3×10^{-3} Pa (vacuum).

X-ray imaging experiments were conducted at the Dynamic Compression Sector (beamline 35-ID) and sector 32 (beamline 32-ID) at the Advanced Photon Source at Argonne National Laboratory. The X-ray source operated in either 324 bunch mode with 22 ps X-ray pulses separated by a 11.47 ns or 24 bunch mode with 33.5 ps X-ray pulses separated by 153 ns between pulses. These X-ray pulse length in both modes are root mean squared pulse durations [28]. In both cases, the detector system was not explicitly synchronized to the X-ray pulse because the phenomena investigated occur on an order of magnitude longer time scale than the pulse spacings. Experiments at 35-ID used the full X-ray spectrum from a U17.2 undulator with a peak energy of approximately 24 keV [24] while experiments at 32-ID used a U18 undulator with roughly the same peak energy. A millisecond X-ray shutter was used to protect the sample and detector system from prolonged X-ray exposure. For detection, the X-rays are converted to visible light by a 100 μm thick LuAG:Ce scintillator (Crytur), which is then diverted out of the X-ray beam path by a silver-coated optical mirror, collected by a long working distance objective lens, and split into four duplicate images by beam splitters (Thor Labs, BSW10R). Each of these four image copies is imaged by a tube lens onto a Princeton Instruments PI-MAX4:1024i iCCD camera. Two different objective and tube lens assemblies were used: a $7.5\times$ magnification, 0.21 NA objective lens (Mitutoyo plan apo infinity corrected long working distance objective, #66-383) paired with a 400 mm effective focal length tube lens yielding $15\times$ total magnification, and a $10\times$, 0.28 NA objective lens (Mitutoyo plan apo infinity corrected long working distance objective, #46-144) paired with a 200 mm effective focal length tube lens yielding $10\times$ total magnification. Raw X-ray absorption image data were reduced to highlight changes in attenuation during the process by dividing the uncorrected absorption image at time t (A_t) by an initial image of the sample collected prior to laser processing (A_0) to obtain a difference image (A_{diff}) using Eq. (1):

$$A_{diff} = \frac{\ln(A_t)}{\ln(A_0)} \quad (1)$$

This procedure generates a difference image A_{diff} where dark regions represent a decrease in X-ray attenuation and light regions represent an increase in X-ray attenuation. In addition to absorption contrast, phase contrast enhances the visibility of material interfaces. The uncertainty of identifying the location of vapor depression edges is approximately 3–5 μm , depending on magnification. Vapor depression geometry was quantified using measurements of depth (D), length at the sample surface (L), and length at half depth (L_h) as illustrated in Fig. 1a. These measurements were used to calculate vapor depression aspect ratio $R = D/L_h$.

Images recorded for Al6061, Ti-64, and 316 L stainless steel were framed such that the surface of the sample plate was clearly observed in the upper half of the image, ideally $\sim 1/4$ of the distance from the top of the image to allow study of the surface and sub-surface regions of the metal. In contrast, the high attenuation of ~ 24 keV photons by Nickel

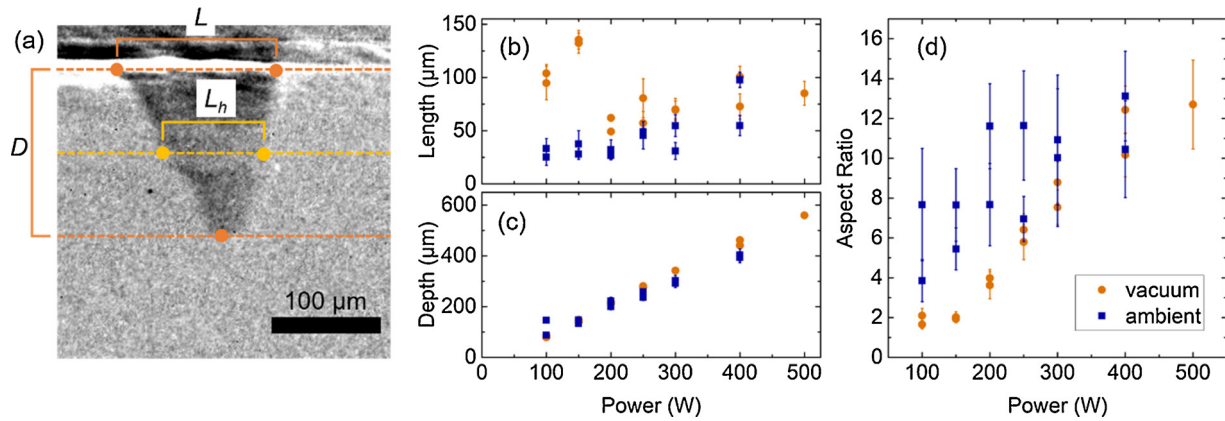


Fig. 1. Vapor depression geometry of 316 L steel as a function of power for 800 mm/s scan speed. (a) Illustration of the three measurements used in this manuscript: vapor depression depth (D) vapor depression surface length (L), and vapor depression length at half depth (L_h). (b) Vapor depression surface length at 1.3×10^{-3} Pa (vacuum) and ~ 97 kPa (ambient). (c) vapor depression depth for both pressures. (d) vapor depression aspect ratio (D/L_h) for both pressures.

400 required framing the surface of the plate with the very top of the image. This geometry permits the extended exposure times required for suitable signal to noise to analyze the sub-surface of Nickel 400 without detector saturation in regions where photons are unattenuated by the sample.

While the solid-liquid interface is not clearly discernable in the *in situ* imaging, optical microscope images of *ex situ* metallographic cross sections were used to quantify the melt pool dimensions for a small subset of samples. These samples were cross-sectioned using a water-cooled, low-speed diamond cut-off saw, and then mounted in epoxy. The samples were then ground using SiC paper down to 1200 grit, and polished using 3 μm and 1 μm polycrystalline diamond suspension. Final vibratory polishing was performed using 0.05 μm colloidal silica. The samples were etched electrolytically using a 10 % oxalic acid solution at 6 V.

3. Results

3.1. Stainless steel melt pool behavior as a function of pressure and oxygen partial pressure

The contrasting vapor depression geometries as a function of laser power between the two pressure regimes are quantified in Fig. 1. In an ambient pressure Ar atmosphere, the *in situ* X-ray imaging of 316 L steel illustrates behavior that is expected based on existing welding literature [5,8,9]. The vapor depression depth (and the corresponding melt pool depth) increases linearly with increasing power (Fig. 1c). During this increase, the vapor depression does not substantially change shape. At the lowest powers, the vapor depression is very shallow, does not extend far in the scan direction, and extends essentially straight downward into the substrate (Fig. 2a). As the laser power increases, both the depth and the length of the vapor depression increase (Fig. 2b). This larger depression remains stable up to ~ 300 W, extending straight downward into the melt pool. Above 300 W, the deeper and longer vapor depression becomes unstable, with ripples moving up and down the back of the vapor depression (Fig. 2c, g). These ripples on the back of the melt pool correlate with small waves on the melt pool surface, similar to behavior observed in welding Al alloys via ultrafast radiography [24]. In addition to the instability of the vapor-liquid interface on the back of the vapor depression, the base of the vapor depression curves backwards. These observations are consistent with literature reports of high-speed optical imaging of laser welding at high velocities as well as reports of additive manufacturing under essentially the same conditions with powder added to the substrate [10,16]. Despite the instabilities observed in the vapor-liquid interface at the melt pool surface, no pores were observed in 316 L steel under the ambient

pressure conditions investigated here.

Under vacuum, the behavior of the steel melt pool exhibits both strong similarities and significant differences relative to those observed under ambient pressure of Ar. The vapor depression depth displays a linear increase with laser power consistent the behavior observed under ambient pressure, and the mean depth values under the two pressure regimes are very similar. *Ex situ* measurements of the melt pool depth are also very similar for the two pressure cases. This behavior is expected for laser welding at reduced pressure at high scan speeds [6]. The identical vapor depression and melt pool depths in this study indicate that the conditions studied here are in the fast welding regime, where the penetration depth is no longer sensitive to the pressure of the cover gas.

While the depth of the vapor depression is consistent between the two pressures, other features of the vapor depression geometry are strikingly different between the two cases. At low powers the length of the vapor depression is much larger at low pressure (Fig. 2d, e) than under ambient conditions (Fig. 2a, b), leading to a low aspect ratio vapor depression. As the laser power increases above 150 W, the wide vapor depression collapses to form a vapor depression that appears similar to what is observed in the ambient pressure case, a deep depression with a high aspect ratio (Fig. 2f) that is closely comparable with the vapor depression under ambient pressure (Fig. 2c). At high powers the vapor depression under vacuum conditions does not exhibit the same ripples at the vapor-liquid interface observed at ambient pressure, and the curve at the bottom of the vapor depression is more pronounced. The vapor depression aspect ratio is consistently higher in the ambient pressure case than the vacuum case. Furthermore, no pore formation is apparent under vacuum, similar to ambient pressure observations.

The *in situ* X-ray images presented here provide information about the depth and length of the vapor depression as a function of processing conditions, but the data do not have sufficient signal to noise to permit an estimate of the width of the vapor depression along the axis of the X-ray beam, perpendicular to the scan direction. Therefore, *ex situ* metallographs of selected conditions in 316 L steel were collected to measure melt pool depth and width as comparisons for vapor depression dimensions. Since melt pool depth correlates strongly with vapor depression depth (Fig. 3a), it is anticipated that melt pool width correlates with vapor depression width. As expected, melt pool widths for both pressures increase with increasing laser power (Fig. 3b). However, melt pools are consistently wider under ambient pressure than in vacuum, indicating that the low aspect ratio, long vapor depression observed at lower powers in the vacuum experiments is not an isotropic expansion of the depression but rather an extension in the scan direction only.

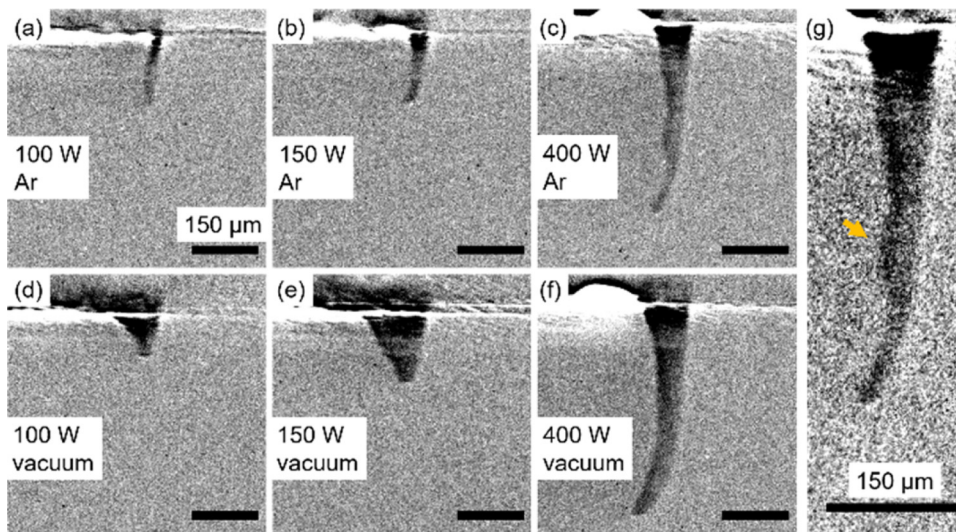


Fig. 2. *In situ* X-ray difference images (A_{diff}) of the vapor depression in 316 L stainless steel with a scan speed of 800 mm/s. Each image represents the change in density relative to the starting sample such that dark regions represent less material and light regions represent more material, with additional phase contrast at material interfaces. These images illustrate ambient pressure behavior of the vapor depression at (a) 100 W, (b) 150 W, and (c) 400 W as well as behavior in vacuum conditions at (d) 100 W, (e) 150 W, and (f) 400 W. Panels (a)–(f) use the same scale. (g) Higher magnification view with adjusted contrast of the vapor depression at 400 W under an Ar atmosphere shown in panel (c). The arrow highlights the instability on the back of the vapor depression.

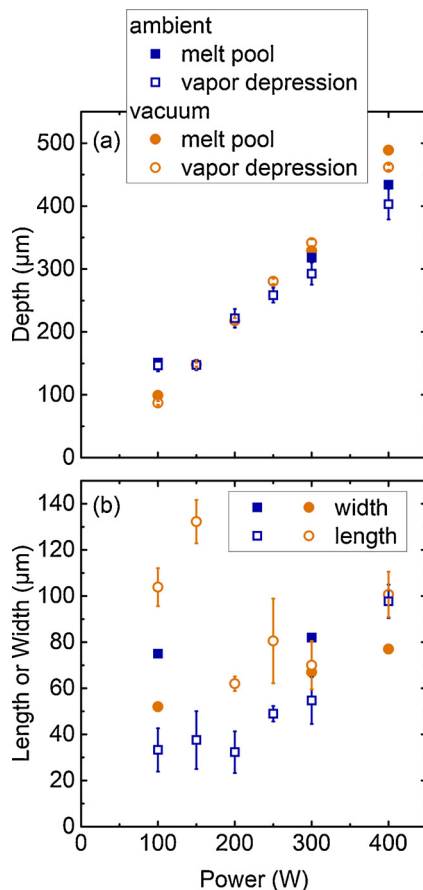


Fig. 3. Comparison of melt pool and vapor depression dimensions in 316 L steel. (a) Vapor depression depth compared with melt pool depth. (b) Vapor depression length compared to melt pool width, measured at the substrate surface. All melt pool dimensions are measured by *ex situ* metallography, while vapor depression measurements are based on *in situ* X-ray imaging.

Fig. 4 illustrates 316 L vapor depression geometries as a function of oxygen partial pressure at ~ 101 kPa with a scan speed of 1000 mm/s. The shape metrics of vapor depression length, depth, and aspect ratio agree quite well in an atmosphere of 10 ppm O_2 case and 13,000 ppm O_2 at 200 W and 300 W. At 400 W, however, the depression is significantly longer and deeper in an atmosphere of 10 ppm O_2 case than in the 13,000 ppm case. This leads to a higher aspect ratio vapor

depression in the 10 ppm O_2 case and the shape is qualitatively different as well, illustrated in Fig. 4d and e.

3.2. Nickel 400 melt pool behavior as a function of pressure

Vapor depression behavior in Nickel 400 for scan speeds of 800 mm/s (Fig. 5) is very similar to what is observed in 316 L steel. The framing of the Ni alloy plate with the surface at the very top of the radiography images described previously can lead to significant errors in measurement of the surface length. Therefore, the length at half depth is used as an alternative measure when discussing the Ni alloy experiments (Fig. 5a). The vapor depression depth exhibits a linear increase with increasing power for both ambient pressure and vacuum. The difference in measured vapor depression depth is quite small between the two cases, with marginally deeper vapor depressions observed at ambient pressure. However, the vapor depression length (and therefore aspect ratio) exhibits significantly different behavior between the two pressures. At ambient pressure, vapor depression length exhibits an approximately linear increase with increasing power, leading to an increase in vapor depression aspect ratio until 250 W, above which the aspect ratio remains relatively constant. Under vacuum, however, vapor depression length increases sharply at low power, reaches a maximum at 200 W and drops slowly at 250 W and above. The result is a transition in the vapor depression aspect ratio starting at 250 W from low to high aspect ratio. This transition is similar to the behavior observed in 316 L steel, but with the transition to a high aspect ratio vapor depression occurring at a higher power in Nickel 400 (Fig. 5c). Vapor depression aspect ratio is consistently higher under ambient pressure than under vacuum.

3.3. Al6061 melt pool behavior as a function of pressure

The behavior observed in Al6061 as a function of pressure (Fig. 6) deviates significantly from the behavior of 316 L steel and Nickel 400. At powers below 200 W, no vapor depression was observed. For both pressures, the vapor depression depth increases linearly as power increases above 200 W. The vapor depression length remains essentially constant as a function of power, although the fluctuations in length (as quantified by the standard deviation of length measurements, represented by error bars in Fig. 6a) are more significant at ambient pressure than under vacuum. The vapor depression aspect ratio at 200 W, the lowest power where a depression is observed, is ~ 11 , significantly higher than the values of 2–4 observed in 316 L and Nickel alloy at low power. This aspect ratio indicates a narrow and deep vapor depression and increases with increasing power. No vapor depression

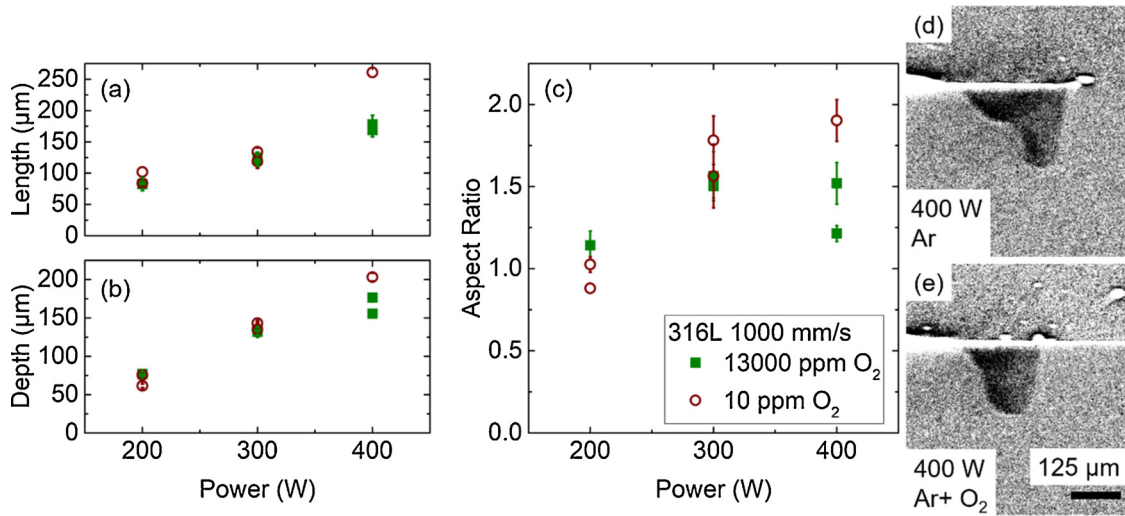


Fig. 4. 316 L steel vapor depression geometry as a function of oxygen partial pressure at 1000 mm/s. (a) Vapor depression length. (b) Vapor depression depth. (c) Vapor depression aspect ratio. (d) Image of the vapor depression produced by a laser power of 400 W in a 10 ppm O₂ environment. (e) Image of the vapor depression produced by a laser power of 400 W in a 13,000 ppm O₂ environment. The scale of panels (d) and (e) is the same.

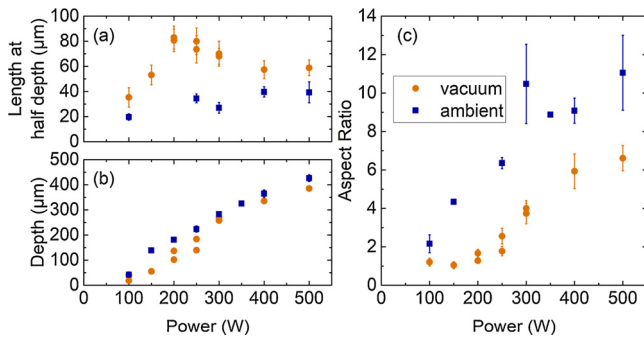


Fig. 5. Vapor depression geometry measurements for Nickel 400 alloy with a scan speed of 800 mm/s. (a) Vapor depression length at half depth, (b) vapor depression depth, and (c) vapor depression aspect ratio, calculated based on length at half depth.

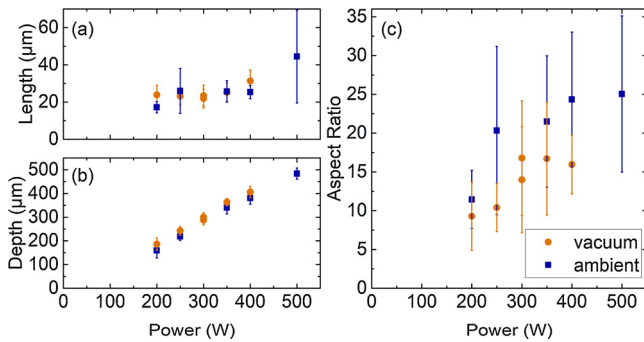


Fig. 6. Vapor depression geometry in Al6061 at a scan speed of 800 mm/s. (a) Vapor depression surface width as a function of power. (b) vapor depression depth as a function of power. (c) Vapor depression aspect ratio as a function of power.

shape transition occurred, in contrast to the behavior in 316 L steel and Nickel 400. Large standard deviations in the aspect ratio (Fig. 6c) arise from fluctuations in the vapor depression length. While aspect ratios for all powers are not significantly different between the vacuum and ambient cases, aspect ratio values for ambient pressure are slightly higher than those observed under vacuum.

3.4. Ti-64 melt pool behavior as a function of pressure and oxygen partial pressure

Vapor depression geometries of Ti-64 at two different scan speeds are illustrated in Fig. 7. At 800 mm/s Ti-64 behaves similarly to what is observed in Al6061, with no distinct transition in vapor depression geometry observed as a function of power. Depth increases linearly with laser power and the depression length again remains essentially constant with power. Furthermore, depression length values exhibit minimal change as a function of power and are similar in both pressure cases. Consequently the aspect ratio is high, above 8 at the lowest point, and increases with increasing power. No transition of the vapor depression shape is observed at this scan speed, and the aspect ratio values for the vacuum and ambient cases are nearly identical.

To investigate the morphology transition in Ti-64 further, the vapor depression geometry as a function of power was measured at a scan speed of 1200 mm/s. These experiments used a slightly larger beam size than the experiments performed at 800 mm/s, $\sim 45 \mu\text{m}$ vs $\sim 55 \mu\text{m}$ beam diameter. As observed at lower scan speeds, depth increases linearly with increasing power, and the difference in overall depth between the two pressures studied here is small. Interestingly, the depression length under vacuum is much larger than at ambient pressure, leading to consistently higher aspect ratios in the ambient pressure case. While a sharp transition in aspect ratio is not observed, the shape of the vapor depression differs between the two pressures in ways that are not well captured by the shape metrics used here. At ambient pressure a kink is present in the rear surface of the vapor depression and is more pronounced at high power (Fig. 7d), while under vacuum the rear surface of the vapor depression is relatively straight (Fig. 7e).

Fig. 8 contrasts the vapor depression geometry for Ti-64 under high purity Ar with a low oxygen content 4 ppm and in an oxygen-rich Ar environment 13,000 ppm. Consistent differences are observed between the two oxygen partial pressures. The vapor depression is longer in the 4 ppm O₂ case, by between 15 % and 30 % at half depth (Fig. 8a) and 40%–180% at the pool surface not shown, although the depression length at melt pool surface exhibits significant fluctuations. The vapor depression depth at 13,000 ppm O₂ is 10%–15% deeper than the vapor depression at 4 ppm O₂ (Fig. 8b), leading to a higher aspect ratio vapor depression at the high O₂ partial pressure (Fig. 8c). In addition to the quantitative differences in the vapor depression size, the melt pool behavior far from the laser impact point is also significantly affected by the change in oxygen partial pressure. In the 4 ppm case (Fig. 8d), the vapor depression looks very similar to what is observed at 1200 mm/s

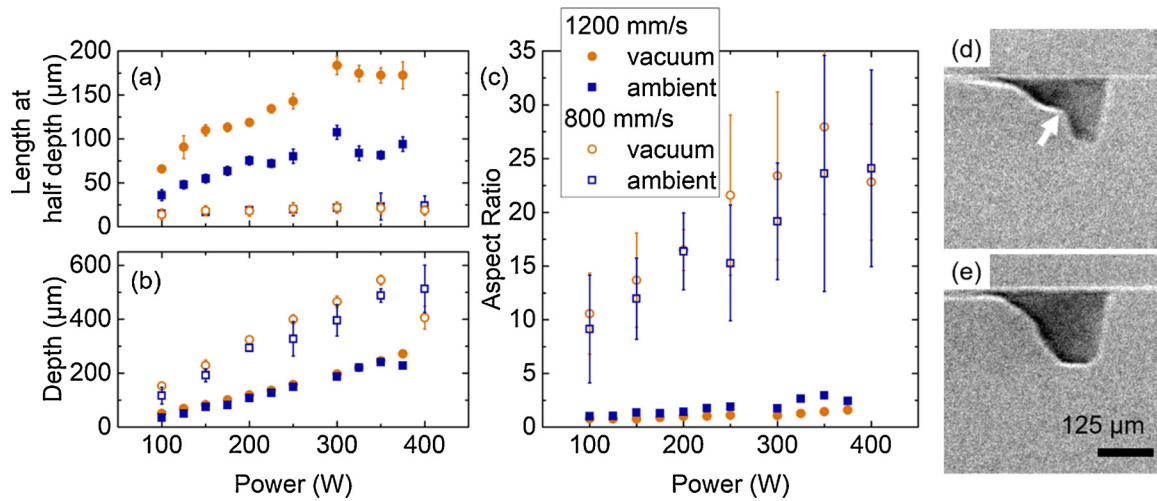


Fig. 7. Ti-64 vapor depression geometry as a function of pressure for both 800 mm/s and 1200 mm/s scan speeds. (a) Vapor depression length at half depth. (b) Vapor depression depth. (c) Vapor depression aspect ratio. (d) Image of the vapor depression produced by a laser power of 250 W and a scan speed of 1200 mm/s at ambient pressure. The white arrow indicates the kink described in the text. (e) Image of the vapor depression produced by a laser power of 250 W and a scan speed of 1200 mm/s under vacuum. The scale of panels (d) and (e) is the same.

in Fig. 7d with a long, shallow tail to the rear of the vapor depression. Under high oxygen partial pressure (Fig. 8e), this tail is not present and instead is replaced by a surface wave that protrudes above the surface of the sample followed by a second, much smaller, depression. This depression, marked with an arrow in Fig. 8e, is observed at both 200 and 300 W at 1000 mm/s and is more pronounced at higher power.

3.5. Surface features of 316 L steel and Nickel 400 weld tracks

An additional contrast between behavior at ambient pressure and under vacuum appears in the formation of surface roughness, or balling, of the melt pool behind the vapor depression. Balling becomes more pronounced at high power (above 150 W) under vacuum but is not observed at ambient pressure, demonstrating that the effect observed by Bidare et al. does not depend on the presence of powder [16]. Fig. 9a illustrates a line profile along the scan direction comparing 316 L tracks produced under both ambient and vacuum conditions with a laser power of 300 W and a scan speed of 800 mm/s. To quantify the periodicity of surface features, we use the 1D fast Fourier transform (FFT) of

the line profile of track height, omitting the start and end of the melt track to avoid artifacts introduced by edge effects. We define the balling length, or distance between peaks in the surface profile of the single track, as the distance corresponding to the highest amplitude peak in the 1D FFT, and use the FFT amplitude as a metric for the strength of balling. Fig. 9b and c show the balling length computed by a 1D FFT of the linear height profile and the mean square amplitude of the FFT peak as a function of power. Balling length under vacuum increases dramatically with power until ~ 200 W and remains relatively constant as power continues to increase. Qualitatively similar balling behavior occurs in the case of Nickel 400 (Fig. 9d and e). At ambient pressure essentially no balling is observed, as indicated by FFT peak magnitudes below 1 for all powers. Under vacuum, balling length is relatively constant at ~ 600 μm for the cases where significant balling occurs. As is the case in steel, a stronger balling tendency is observed with increased power. While the onset of strong balling under vacuum coincides with the collapse of the vapor depression length in 316 L steel (Fig. 1b), the vapor depression collapse does not occur at the same power as the onset of strong balling in Nickel 400 so these phenomena

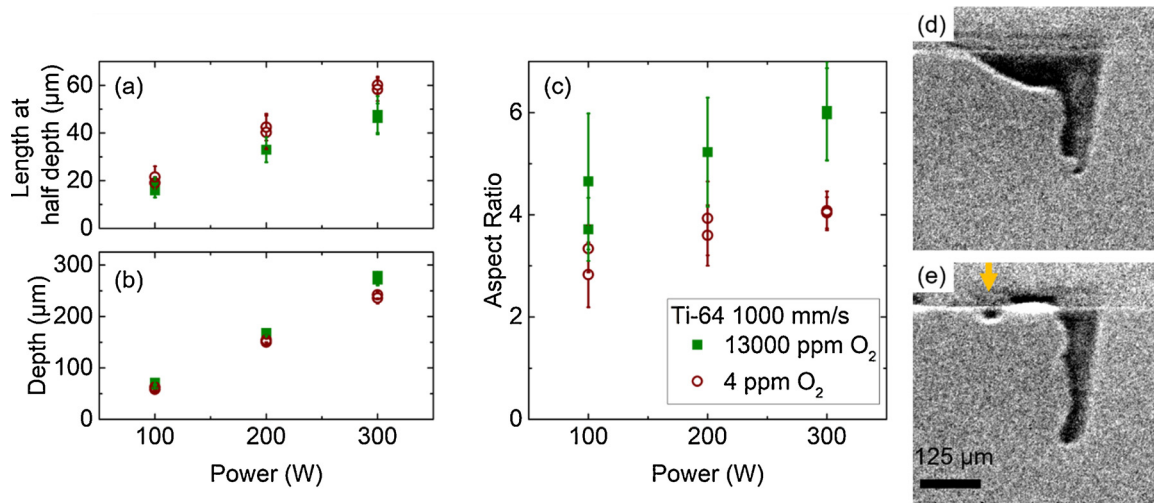


Fig. 8. Ti-64 vapor depression geometry as a function of oxygen partial pressure at 1000 mm/s. (a) Vapor depression length at half depth. (b) Vapor depression depth. (c) Vapor depression aspect ratio at half depth. (d) Image of the vapor depression produced by a laser power of 300 W in a 4 ppm O₂ environment. (e) Image of the vapor depression produced by a laser power of 300 W in a 13,000 ppm O₂ environment, with the second depression far from the laser focus location marked with an arrow. The scale of panels (d) and (e) is the same.

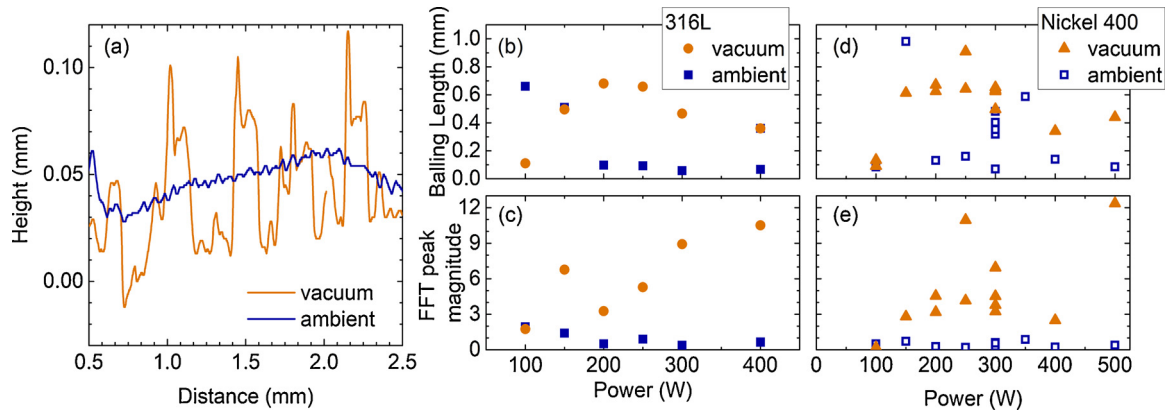


Fig. 9. Surface features of melted tracks in 316 L steel. (a) Compared line profiles of vacuum and ambient melt tracks produced with 300 W laser power and 800 mm/s scan speed in 316 L. (b) balling lengths as a function of power for 316 L at a scan speed of 800 mm/s. (c) the magnitude of the FFT peak corresponding to the balling lengths shown in panel (b). (d) balling lengths as a function of power for Nickel 400 at a scan speed of 800 mm/s. (e) the magnitude of the FFT peak corresponding to the balling lengths shown in panel (d).

are likely not causally linked.

4. Discussion

The vapor depression shape at both pressures is determined by the combination of melt pool surface tension and the interaction of the metal vapor jet with the surface of the melt pool. The metal vapor jet is ejected from the melt pool where the laser hits the melt pool surface and is directed in the direction opposite the laser scan vector at an angle determined by the laser scan speed and the angle of the front surface of the vapor depression [14,25,29,30]. Recoil pressure from the vapor jet pushes the liquid metal surface down into the melt pool, creating a vapor depression. Recoil pressure is given by Eq. (2), which is derived from kinetic theory [31]:

$$P_r = P^* e^{\lambda \left(\frac{1}{T_b} - \frac{1}{T_s} \right)} \quad (2)$$

Where P_r is the recoil pressure, P^* is ambient pressure, λ is the evaporation energy, T_b is the equilibrium boiling point of the liquid at P^* , and T_s is the surface temperature of the liquid metal. The metal vapor ejected by the vapor jet impacts the rear wall of this vapor depression, forcing it backwards and causing the vapor depression to lengthen. The length of the vapor depression is determined by the balance between the momentum transferred from the metal vapor jet to the liquid surface and the surface tension of the liquid metal. It is also influenced by the stability of the curved liquid metal surface itself, which is proportional to surface energy expressed as the closing pressure of the keyhole P_c [13,32]

$$P_c \sim \frac{\gamma}{a} \quad (3)$$

Where γ represents specific surface energy and a represents the curvature of the melt pool surface, which is proportional to the laser spot size and also influenced by the shape of the vapor depression. In this formalism, curvature a is inversely related to the radius of curvature of the liquid surface, such that $a = 0$ for a perfectly flat surface.

At low power, the vapor depression is much longer under vacuum conditions than under ambient conditions. This primarily arises because of the difference in melt pool surface temperature and therefore surface tension, which leads to an increase in the laser power required to produce sufficient vapor recoil pressure to overcome P_c . At reduced pressures the boiling point of the metal under thermodynamic equilibrium decreases as described by the Clausius-Clapeyron equation [16,33]:

$$\ln \left(\frac{P_2}{P_1} \right) = \frac{L_{vap}}{R} \left(\frac{1}{T_1} - \frac{1}{T_2} \right) \quad (4)$$

Where L_{vap} is the latent heat of vaporization, R is the ideal gas constant, and (P_1, T_1) and (P_2, T_2) are two points on the vaporization/condensation boundary of the pressure – temperature phase diagram. Since the temperature of the melt pool is limited by evaporative cooling [15], the reduced boiling temperature reduces the peak temperature of the melt pool and therefore surface temperatures throughout the melt. These temperature changes are quite significant: in the case of 316 L steel the equilibrium boiling point drops from ~ 3090 K at 101.3 kPa [16,34] to ~ 1463 K at 1.3×10^{-3} Pa. The actual peak temperature of the melt surface is likely higher in both cases due to non-equilibrium superheating and local pressure effects, but these estimates provide a reasonable approximation of the temperature differences in the melt pool for the two cases. In the liquid metals investigated in this study, surface tension decreases linearly as a function of temperature [35]. The melt pool under vacuum therefore has a higher surface tension than under ambient conditions. The higher surface tension forces the melt pool surface towards a flatter geometry, which manifests as a low aspect ratio vapor depression. This shape reduces the surface energy by reducing the curvature of the melt pool surface in the vapor depression. In terms of Eq. (3), this corresponds to a decrease in γ at reduced pressure, which leads to lower a for a given P_c . At sufficiently high power, the local pressure at the bottom of the vapor depression is dominated by the metal vapor flux from the vapor jet. Above this critical laser power, which is different for each material, surface tension effects are less important and the high local vapor pressure creates a deep, high aspect ratio keyhole. Above this critical laser power the geometry difference between the vacuum and ambient cases is small, as observed in the strong similarities between the high power conditions under both pressure regimes (Figs. 1d, 5 c, 6 c, 7 c). In spite of these similarities, most materials still exhibit a slightly higher aspect ratio vapor depression in the ambient pressure case when compared to vacuum. In addition to surface tension, temperature has a strong influence on the viscosity of the melt pool. In the case of 316 L steel, the change in melt pool surface temperatures due to the lower boiling point leads to greater than fivefold increase of viscosity if the liquid [34]. Therefore, the melt pool under vacuum conditions requires a greater recoil force to deform fluid flow and develop a high aspect ratio vapor depression. While the recoil pressure and therefore metal vapor flux are both lower in the vacuum case, the mean free path of the metal vapor in vacuum is much longer than at ambient pressure.

The introduction of oxygen in the cover gas has a significant effect on the flow behavior near the vapor depression, because even small increases in oxygen content lead to large decreases in the surface tension of liquid metals [36,37]. Vapor depression morphology changes between low ~ 10 ppm and high 13,000 ppm oxygen partial pressure in both Ti-64 and 316 L steel, although the magnitude of these changes

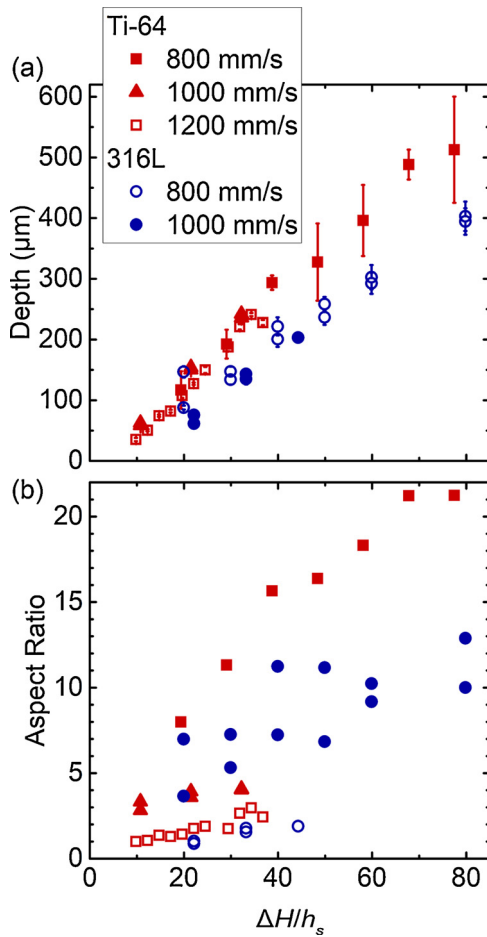


Fig. 10. Comparison of vapor depression shapes as a function of normalized enthalpy. (a) Vapor depression depth of 316 L and Ti-64 plotted as a function of normalized enthalpy. (b) Vapor depression aspect ratio plotted as a function of normalized enthalpy.

varies significantly between the two materials. In Ti-64, morphological differences associated with the two oxygen levels were observed at all laser powers and scan speeds investigated (Fig. 8), with higher oxygen content leading to a higher aspect ratio vapor depression. In 316 L, however, differences in melt pool morphology only became pronounced at 400 W (at 1000 mm/s), the highest power level investigated (Fig. 4). The magnitude of this effect varies from metal to metal due to the varying oxygen affinity between metal alloys. A precise description of this observation is complicated by the fact that surface tension has a non-monotonic relationship with temperature for some levels of oxygen contamination [36], and the exact oxygen content of the material is influenced significantly by surface oxidation prior to laser melting. The fine details of this vapor depression behavior as a function of oxygen content becomes even more difficult to predict in a full-scale LPBF build, where control of surface oxidation and moisture uptake of the feedstock powder is a significant challenge. Within the scope of Eq. (3), for a given pressure, the presence of oxygen increases γ , thereby increasing the curvature of the vapor depression α and leading to higher vapor depression aspect ratios.

In addition to quantitative differences in vapor depression size, oxygen partial pressure also causes changes in the melt flow behavior that are not captured by vapor depression size measurements. These changes are most clear in Ti-64, the more oxygen-sensitive of the two metals. Fig. 8d and e illustrates the development of a small surface wave followed by a relatively shallow secondary depression, $\sim 30 \mu\text{m}$ deep and $\sim 100 - 150 \mu\text{m}$ behind the back of the primary vapor depression, in the oxygen poisoned case but not the Ar case. This

secondary depression is not formed due to recoil pressure but is instead formed due to changes to the melt pool flow induced by changes in the local surface tension of the oxygen-reacted melt surface. This secondary depression is remarkably stable, appearing constantly with some fluctuation at 200 W and 300 W in high oxygen content environments for Ti-64. Notably, this feature is not present in the pure Ar case, so it is apparently stabilized by the oxygen rich atmosphere. This discrepancy highlights the influence of the surface tension of the metal on vapor depression geometry, as oxygen contamination only influences the surface tension of the melt pool, not the magnitude of recoil pressure or surface temperature of the melt.

We speculate that the formation of the secondary depression is driven by a peak in the local surface tension of the melt immediately behind the vapor depression due to a balance between temperature effects and oxygen saturation effects. Oxygen transport into the vapor depression itself is limited by the metal vapor flux from evaporative cooling, so oxygen uptake on the metal surface becomes much more pronounced on the melt pool surface behind the vapor depression than in the depression itself. Moving backwards from the vapor depression, the temperature of the melt pool falls, increasing surface tension. However, the oxygen content of the surface simultaneously increases, which decreases surface tension. This balance leads to a peak in surface tension shortly behind the vapor depression, which pulls in nearby liquid to form a small bump in the melt pool surface immediately behind the vapor depression, and also forming the secondary depression behind it (Fig. 8e).

The laser power threshold for the transition between the low aspect-ratio vapor depression observed at low power and the high aspect-ratio depression observed at high power varies based on the material. This behavior is expected, because the shape of the vapor depression is primarily influenced by liquid vaporization energy, surface tension, and viscosity of the liquid metal near the boiling point. These parameters vary significantly from material to material, so the threshold powers for vapor depression behavior will be material-dependent. One formalism for comparing laser melting parameters across different materials is the normalized enthalpy approach, which uses a scaling law to account for different materials properties [2,27,38–40] given by Eq. (5):

$$\frac{\Delta H}{h_s} = \frac{AP}{\pi \rho C T_m \sqrt{D} u r^3} \quad (5)$$

Where ΔH is the specific enthalpy of melting, h_s is the enthalpy at melting, A is material absorptivity, P is the laser power, ρ is the material density, C is the specific heat capacity, T_m is the equilibrium melting temperature, D is the thermal diffusivity, u is scan speed, and r is the $1/e$ radius of the laser. Since normalized enthalpy has been successfully used to predict the keyhole transition threshold at ambient pressure in Ti-64, Inconel alloys, and 316 L [38], it is expected to capture the observed morphology transition. A comparison of the parameters used for Ti-64 and 316 L is shown in Fig. 10. Nickel 400 is omitted from this comparison because not all of the required materials properties are available to compute normalized enthalpy. The normalized enthalpy scaling predicts vapor depression depth (Fig. 10a), although with a greater spread of the data than was observed by Ye et al [38]. This slight discrepancy may be because of a slight systematic difference in the relationship between vapor depression depth and melt pool depth in Ti-64 and 316 L steel. However, the normalized enthalpy scaling does not predict changes in the vapor depression shape, even within a single material such as Ti-64 (Fig. 10b). This is because the shape of the vapor depression depends on variables that are not explicitly accounted for in the normalized enthalpy scaling, which was developed primarily to predict melt pool shape rather than the shape of the vapor depression. The most important factors not accounted for in the normalized enthalpy scaling are the surface tension of the liquid and the change in angle of the front wall of the vapor depression as a function of scan speed, which is known to heavily influence the vapor depression

geometry [25].

Effects caused by changes in surface tension and melt viscosity are also evident in the high-power regime, above the power threshold for the vapor depression geometry transition in the vacuum case. In both Nickel alloy and 316L, the vacuum conditions exhibit significant balling behavior. This arises due to the formation of waves on the surface of the melt pool due to fluid flow effects enabled by the lower surface temperature, and consequently higher surface tension, under vacuum that do not occur under ambient pressure. As reported by Bidare et al. [16], this balling is not caused by the Raleigh-Plateau instability but rather by waves formed by changes to the melt pool flow near the edges of the melt pool. The mechanism that causes this large scale, periodic balling is distinct from much finer surface features described by Martin *et al* that correlate with instabilities on the back wall of the vapor depression [24].

While the vapor depression length differs between the vacuum case and the ambient case at low powers, the vapor depression and melt pool depths for the two pressures are the same within experimental uncertainties. Such close comparison indicates that the balance between vapor recoil pressure, which exerts a downward force on the liquid surface to form the vapor depression, and surface tension, which exerts an opposing force on the liquid surface, does not change significantly between vacuum and ambient. This contrasts with reported behavior at lower scan speeds, where reduced pressure increases weld penetration depths by as much as a factor of two [5].

A possible alternate explanation is that under vacuum, the vapor jet expands uniformly, becoming less directional than what is observed at ambient pressure. If this were the case, the vapor depression is expected to be wider perpendicular to the scan direction under vacuum in addition to the lengthening observed via X-ray imaging. As illustrated by Fig. 3, the melt pools are consistently wider for the ambient case than for the vacuum case. This behavior suggests that uniform gas expansion does not have a strong influence on the vapor depression geometry, and that the surface temperature of the melt pool under vacuum is lower than at ambient pressure. Therefore, we discount the possibility that uniform gas expansion of the metal vapor plays a significant role in causing the change in vapor depression geometry between vacuum and ambient pressure.

5. Conclusions

This article reports the melt pool flow behavior during laser melting as a function of the process atmosphere pressure and composition. At low energy density, significantly different vapor depression morphologies are observed under vacuum and ambient pressure conditions while at high energy densities the vapor depression morphology very similar under vacuum and ambient pressure. These differences in surface geometry are best quantified by the vapor depression aspect ratio. This behavior was observed in 316 L steel, Nickel 400, and Ti-64 but not in Al6061. The details of the behavior and magnitude of the change as a function of power vary depending on material and scan speed. We attribute these differences primarily to changes in the surface tension of the liquid metal. The surface tension changes because the boiling temperature, and therefore melt pool surface temperature, are lower at reduced pressure. We also observe contrasting flow behavior in cases where the atmosphere has a significant O₂ partial pressure when compared to a pure Ar atmosphere, and also attribute these changes primarily to the influence of oxygen uptake on liquid metal surface tension. The subsurface observations reported here complement previous optical experiments and modelling studies and further improve our understanding of the physics of the laser-material interactions central to both LPBF and laser welding.

CRedit authorship contribution statement

Nicholas P. Calta: Conceptualization, Formal analysis,

Investigation, Writing - original draft, Visualization, Methodology. **Aiden A. Martin:** Conceptualization, Formal analysis, Investigation, Writing - review & editing, Software, Methodology. **Joshua A. Hammons:** Conceptualization, Formal analysis, Investigation, Writing - review & editing, Software. **Michael H. Nielsen:** Investigation, Writing - review & editing. **Tien T. Roehling:** Investigation, Writing - review & editing. **Kamel Fezzaa:** Writing - review & editing, Resources. **Manyalibo J. Matthews:** Conceptualization, Writing - review & editing. **Jason R. Jeffries:** Conceptualization, Writing - review & editing. **Trevor M. Willey:** Conceptualization, Writing - review & editing, Investigation, Funding acquisition. **Jonathan R.I. Lee:** Conceptualization, Writing - review & editing, Investigation, Supervision, Project administration, Funding acquisition.

Declaration of Competing Interest

The authors declare that they have no known competing financial interests or personal relationships that could have appeared to influence the work reported in this paper.

Acknowledgements

This work was performed under the auspices of the U.S. Department of Energy (DOE) by Lawrence Livermore National Laboratory (LLNL) under Contract No. DE-AC52-07NA27344. This publication is based upon work performed at the Dynamic Compression Sector (DCS), which is operated by Washington State University under the U.S. Department of Energy/National Nuclear Security Administration award no. DE-NA0002442. This research used resources of the Advanced Photon Source, a DOE Office of Science User Facility operated for the DOE Office of Science by Argonne National Laboratory under contract no. DE-AC02-06CH11357. The authors gratefully acknowledge valuable discussions with W. King, S. Khairallah, and A. Rubenchik, sample preparation by the LLNL Precision Machine Shop, and beamtime support from N. Sinclair, P. Rigg, D. Rickerson, J. Klug, and N. Weir at DCS and A. Deriy at APS sector 32. LLNL-JRNL-788222. Funding: The work was supported by the LDRD Program at LLNL [project 17-ERD-042].

References

- [1] *Wholers Report*, Wholers Associates, Fort Collins, CO, 2019.
- [2] W.E. King, H.D. Barth, V.M. Castillo, G.F. Gallegos, J.W. Gibbs, D.E. Hahn, C. Kamath, A.M. Rubenchik, Observation of keyhole-mode laser melting in laser powder-bed fusion additive manufacturing, *J. Mater. Process. Technol.* 214 (2014) 2915–2925, <https://doi.org/10.1016/j.jmatprotec.2014.06.005>.
- [3] Y. Arata, N. Abe, T. Oda, N. Tsujii, Fundamental phenomena during vacuum laser welding, *ICALEO 1984* (1984) 1–7, <https://doi.org/10.2351/1.5057605>.
- [4] C. Börner, K. Dilger, V. Rominger, T. Harter, T. Krüssel, T. Löwer, Influence of ambient pressure on spattering and weld seam quality in laser beam welding with the solid-state laser, *ICALEO 2011* (2011) 621–629, <https://doi.org/10.2351/1.5062302>.
- [5] Y. Abe, M. Mizutani, Y. Kawahito, S. Katayama, Deep penetration welding with high power laser under vacuum, *ICALEO 2010* (2010) 648–653, <https://doi.org/10.2351/1.5062094>.
- [6] S. Pang, K. Hirano, R. Fabbro, T. Jiang, Explanation of penetration depth variation during laser welding under variable ambient pressure, *J. Laser Appl.* 27 (2015) 022007, <https://doi.org/10.2351/1.4913455>.
- [7] M. Miyagi, Y. Kawahito, H. Wang, H. Kawakami, T. Shoubu, M. Tsukamoto, X-ray phase contrast observation of solidification and hot crack propagation in laser spot welding of aluminum alloy, *Opt. Express* 26 (2018) 22626–22636, <https://doi.org/10.1364/OE.26.022626>.
- [8] M. Miyagi, Y. Kawahito, H. Kawakami, T. Shoubu, Dynamics of solid-liquid interface and porosity formation determined through x-ray phase-contrast in laser welding of pure Al, *J. Mater. Process. Technol.* 250 (2017) 9–15, <https://doi.org/10.1016/j.jmatprotec.2017.06.033>.
- [9] Y. Kawahito, H. Wang, In-situ observation of gap filling in laser butt welding, *Scr. Mater.* 154 (2018) 73–77, <https://doi.org/10.1016/j.scriptamat.2018.05.033>.
- [10] M. Zhang, G. Chen, Y. Zhou, S. Li, Direct observation of keyhole characteristics in deep penetration laser welding with a 10 kW fiber laser, *Opt. Express* 21 (2013) 19997–20004, <https://doi.org/10.1364/OE.21.019997>.
- [11] M. Chen, Y. Wang, G. Yu, D. Lan, Z. Zheng, In situ optical observations of keyhole dynamics during laser drilling, *Appl. Phys. Lett.* 103 (2013) 194102, <https://doi.org/10.1063/1.4829147>.

- [12] H. Wang, M. Nakanishi, Y. Kawahito, Dynamic balance of heat and mass in high power density laser welding, *Opt. Express* 26 (2018) 6392–6399, <https://doi.org/10.1364/OE.26.006392>.
- [13] R. Fabbro, K. Hirano, S. Pang, Analysis of the physical processes occurring during deep penetration laser welding under reduced pressure, *J. Laser Appl.* 28 (2016) 022427, <https://doi.org/10.2351/1.4944002>.
- [14] S. Ly, A.M. Rubenchik, S.A. Khairallah, G. Guss, M.J. Matthews, Metal vapor micro-jet controls material redistribution in laser powder bed fusion additive manufacturing, *Sci. Rep.* 7 (2017), <https://doi.org/10.1038/s41598-017-04237-z>.
- [15] S.A. Khairallah, A.T. Anderson, A. Rubenchik, W.E. King, Laser powder-bed fusion additive manufacturing: physics of complex melt flow and formation mechanisms of pores, spatter, and denudation zones, *Acta Mater.* 108 (2016) 36–45, <https://doi.org/10.1016/j.actamat.2016.02.014>.
- [16] P. Bidare, I. Bitharas, R.M. Ward, M.M. Attallah, A.J. Moore, Laser powder bed fusion at sub-atmospheric pressures, *Int. J. Mach. Tools Manuf.* 130–131 (2018) 65–72, <https://doi.org/10.1016/j.ijmactools.2018.03.007>.
- [17] M.J. Matthews, G. Guss, S.A. Khairallah, A.M. Rubenchik, P.J. Depond, W.E. King, Denudation of metal powder layers in laser powder bed fusion processes, *Acta Mater.* 114 (2016) 33–42, <https://doi.org/10.1016/j.actamat.2016.05.017>.
- [18] Y. Kawahito, Y. Uemura, Y. Doi, M. Mizutani, K. Nishimoto, H. Kawakami, M. Tanaka, H. Fujii, K. Nakata, S. Katayama, Elucidation of the effect of welding speed on melt flows in high-brightness and high-power laser welding of stainless steel on basis of three-dimensional X-ray transmission observation, *Weld. Int.* 31 (2016) 206–213, <https://doi.org/10.1080/09507116.2016.1223204>.
- [19] N.P. Calta, J. Wang, A.M. Kiss, A.A. Martin, P.J. Depond, G.M. Guss, V. Thampy, A.Y. Fong, J.N. Weker, K.H. Stone, C.J. Tassone, M.J. Kramer, M.F. Toney, A. Van Buuren, M.J. Matthews, An instrument for in situ time-resolved X-ray imaging and diffraction of laser powder bed fusion additive manufacturing processes, *Rev. Sci. Instrum.* 89 (2018) 055101, <https://doi.org/10.1063/1.5017236>.
- [20] C. Zhao, K. Fezzaa, R.W. Cunningham, H. Wen, F. De Carlo, L. Chen, A.D. Rollett, T. Sun, Real-time monitoring of laser powder bed fusion process using high-speed X-ray imaging and diffraction, *Sci. Rep.* 7 (2017), <https://doi.org/10.1038/s41598-017-03761-2>.
- [21] C.L.A. Leung, S. Marussi, R.C. Atwood, M. Towrie, P.J. Withers, P.D. Lee, In situ X-ray imaging of defect and molten pool dynamics in laser additive manufacturing, *Nat. Commun.* 9 (2018), <https://doi.org/10.1038/s41467-018-03734-7>.
- [22] F. Abt, M. Boley, R. Weber, T. Graf, G. Popko, S. Nau, Novel X-ray system for in-situ diagnostics of laser based processes – first experimental results, *Phys. Procedia* 12 (2011) 761–770, <https://doi.org/10.1016/j.phpro.2011.03.095>.
- [23] A. Matsunawa, N. Seto, J.-D. Kim, M. Mizutani, S. Katayama, Dynamics of keyhole and molten pool in high-power CO2 laser welding, in: *high-Power Lasers in Manufacturing*, Int. Soc. Opt. Photonics (2000) 34–46, <https://doi.org/10.1117/12.377006>.
- [24] A.A. Martin, N.P. Calta, J.A. Hammons, S.A. Khairallah, M.H. Nielsen, R.M. Shuttlesworth, N. Sinclair, M.J. Matthews, J.R. Jeffries, T.M. Willey, J.R.I. Lee, Ultrafast dynamics of laser-metal interactions in additive manufacturing alloys captured by in situ X-ray imaging, *Mater. Today Adv.* 1 (2019) 100002, <https://doi.org/10.1016/j.mtadv.2019.01.001>.
- [25] R. Cunningham, C. Zhao, N. Parab, C. Kantzos, J. Pauza, K. Fezzaa, T. Sun, A.D. Rollett, Keyhole threshold and morphology in laser melting revealed by ultrahigh-speed x-ray imaging, *Science* 363 (2019) 849–852, <https://doi.org/10.1126/science.aav4687>.
- [26] Q. Guo, C. Zhao, L.I. Escano, Z. Young, L. Xiong, K. Fezzaa, W. Everhart, B. Brown, T. Sun, L. Chen, Transient dynamics of powder spattering in laser powder bed fusion additive manufacturing process revealed by in-situ high-speed high-energy x-ray imaging, *Acta Mater.* 151 (2018) 169–180, <https://doi.org/10.1016/j.actamat.2018.03.036>.
- [27] A.A. Martin, N.P. Calta, S.A. Khairallah, J. Wang, P.J. Depond, A.Y. Fong, V. Thampy, G.M. Guss, A.M. Kiss, K.H. Stone, C.J. Tassone, J.N. Weker, M.F. Toney, T. van Buuren, M.J. Matthews, Dynamics of pore formation during laser powder bed fusion additive manufacturing, *Nat. Commun.* 10 (2019) 1987, <https://doi.org/10.1038/s41467-019-10009-2>.
- [28] M. Borland, G. Decker, L. Emery, W. Guo, K. Harkay, V. Sajaev, C.-Y. Yao, APS Storage Ring Parameters, n.d. <https://ops.aps.anl.gov/SRparameters/> (accessed September 10, 2019).
- [29] N. Kouraytem, X. Li, R. Cunningham, C. Zhao, N. Parab, T. Sun, A.D. Rollett, A.D. Spear, W. Tan, Effect of laser-matter interaction on molten pool flow and keyhole dynamics, *Phys. Rev. Appl.* 11 (2019) 064054, <https://doi.org/10.1103/PhysRevApplied.11.064054>.
- [30] C. Zhao, Q. Guo, X. Li, N. Parab, K. Fezzaa, W. Tan, L. Chen, T. Sun, Bulk-explosion-Induced metal spattering during laser processing, *Phys. Rev. X* 9 (2019) 021052, <https://doi.org/10.1103/PhysRevX.9.021052>.
- [31] D. Bauerle, *Laser Processing and Chemistry*, Springer, 2011.
- [32] J. Trapp, A.M. Rubenchik, G. Guss, M.J. Matthews, In situ absorptivity measurements of metallic powders during laser powder-bed fusion additive manufacturing, *Appl. Mater. Today* 9 (2017) 341–349, <https://doi.org/10.1016/j.apmt.2017.08.006>.
- [33] P. Atkins, J. De Paula, *Physical Chemistry*, 8th ed., W. H. Freeman and Company, New York, 2006.
- [34] C.S. Kim, *Thermophysical Properties of Stainless Steels*, Argonne National Laboratory, 1975.
- [35] I. Egry, E. Ricci, R. Novakovic, S. Ozawa, Surface tension of liquid metals and alloys — recent developments, *Adv. Colloid Interface Sci.* 159 (2010) 198–212, <https://doi.org/10.1016/j.cis.2010.06.009>.
- [36] A.E. Gheribi, P. Chartrand, Temperature and oxygen adsorption coupling effects upon the surface tension of liquid metals, *Sci. Rep.* 9 (2019) 7113, <https://doi.org/10.1038/s41598-019-43500-3>.
- [37] S. Ozawa, K. Morohoshi, T. Hibiya, H. Fukuyama, Influence of oxygen partial pressure on surface tension of molten silver, *J. Appl. Phys.* 107 (2010) 014910, <https://doi.org/10.1063/1.3275047>.
- [38] J. Ye, S.A. Khairallah, A.M. Rubenchik, M.F. Crumb, G. Guss, J. Belak, M.J. Matthews, Energy coupling mechanisms and scaling behavior associated with laser powder bed fusion additive manufacturing, *AdvEngMater.* 21, 2019, 1900185, <https://doi.org/10.1002/adem.201900185>.
- [39] A.M. Rubenchik, W.E. King, S.S. Wu, Scaling laws for the additive manufacturing, *J. Mater. Process. Technol.* 257 (2018) 234–243, <https://doi.org/10.1016/j.jmatprotec.2018.02.034>.
- [40] D.B. Hann, J. Iammi, J. Folkes, A simple methodology for predicting laser-weld properties from material and laser parameters, *J. Phys. D Appl. Phys.* 44 (2011) 445401, <https://doi.org/10.1088/0022-3727/44/44/445401>.